

Phase-sensitive optical coherence tomography characterization of pulse-induced trabecular meshwork displacement in *ex vivo* nonhuman primate eyes

Peng Li
Roberto Reif
Zhongwei Zhi
Elizabeth Martin
Tueng T. Shen
Murray Johnstone
Ruikang K. Wang

Phase-sensitive optical coherence tomography characterization of pulse-induced trabecular meshwork displacement in *ex vivo* nonhuman primate eyes

Peng Li,^{a#} Roberto Reif,^{a#} Zhongwei Zhi,^{a#} Elizabeth Martin,^b Tueng T. Shen,^{a,b} Murray Johnstone,^b and Ruikang K. Wang^{a,b}

^aUniversity of Washington, Departments of Bioengineering, Seattle, Washington 98195

^bUniversity of Washington, Department of Ophthalmology, Seattle, Washington 98104

Abstract. Glaucoma is a blinding disease for which intraocular pressure (IOP) is the only treatable risk factor. The mean IOP is regulated through the aqueous outflow system, which contains the trabecular meshwork (TM). Considerable evidence indicates that trabecular tissue movement regulates the aqueous outflow and becomes abnormal during glaucoma; however, such motion has thus far escaped detection. The purpose of this study is to describe a novel use of a phase-sensitive optical coherence tomography (PhS-OCT) method to assess pulse-dependent TM movement. For this study, we used enucleated monkey eyes, each mounted in an anterior segment holder. A perfusion system was used to control the mean IOP as well as to provide IOP sinusoidal transients (amplitude 3 mmHg, frequency 1 pulse/second) in all experiments. Measurements were carried out at seven graded mean IOPs (5, 8, 10, 20, 30, 40, and 50 mm Hg). We demonstrate that PhS-OCT is sensitive enough to image/visualize TM movement synchronous with the pulse-induced IOP transients, providing quantitative measurements of dynamic parameters such as velocity, displacement, and strain rate that are important for assessing the biomechanical compliance of the TM. We find that the largest TM displacement is in the area closest to Schlemm's canal (SC) endothelium. While maintaining constant ocular pulse amplitude, an increase of mean IOP results in a decrease of TM displacement and mean size of the SC. These results demonstrate that the PhS-OCT is a useful imaging technique capable of assessing functional properties necessary to maintain IOP in a healthy range, offering a new diagnostic alternative for glaucoma. © 2012 Society of Photo-Optical Instrumentation Engineers (SPIE). [DOI: 10.1117/JBO.17.7.076026]

Keywords: optical coherence tomography; aqueous; trabecular meshwork; Schlemm's canal; glaucoma; pulsatile flow.

Paper 12261 received May 1, 2012; revised manuscript received Jun. 19, 2012; accepted for publication Jul. 2, 2012; published online Jul. 24, 2012.

1 Introduction

Glaucoma, the second leading cause of irreversible blindness,¹ is defined as an optic neuropathy of unknown etiology characterized by optic nerve damage, which results in visual field loss. Currently, direct assessment of the damage to the visual system is the primary means for diagnosing glaucoma and determining the need for escalation of therapy.² However, current treatment techniques are frequently associated with continued progression of visual system damage. For example, in eyes of patients managed with standard glaucoma therapy, one study with a 20-year follow-up found the risk of legal blindness to be 27%.³ In another study with a 15-year follow-up, 68% of eyes had progressive damage and 27% became legally blind.⁴

Deterioration in visual function is detected by visual fields. Progressive deterioration in the microstructures of the visual system can be detected by several modalities, with the least complex being the ophthalmoscope and photography. Optical coherence tomography (OCT) maps the contour of the optic nerve head, the peripapillary nerve fiber layer, and the ganglion cell complex.⁵⁻¹⁴ Scanning laser polarimetry is often used to assess polarization of retinal nerve fibers,^{11,15-17} whereas, scanning

laser tomography is used to measure the surface contour of the optic nerve head.¹⁸⁻²⁰ However, changes in the parameters measured represent evidence of permanent damage to the visual system.

The one treatable problem that minimizes or stops progression of the glaucoma process is the regulation of intraocular pressure (IOP) within a narrow range.²¹ Clinical measurements of IOP are typically done three to four times a year, with each measurement taking about 3 s that provide about 12 s of IOP sampling per year. Blinking and eye movements induce IOP transients of ≥ 10 mmHg that occur numerous times each minute.²² Measurements of IOP do not capture these transients because they are acquired while the patient is looking straight ahead without blinking or eye movement. Marked diurnal fluctuations of IOP are also well recognized but not practical to measure.^{23,24} In addition, IOP spontaneously varies from day to day.^{25,26}

The difficulty in gaining a true assessment of IOP fluctuation over time limits its ability to predict progressive glaucoma damage,²⁷ leaving us with progressive visual field²⁸ and structural damage^{29,30} to the visual system as a primary diagnostic tool for treatment guidance. Currently there is no method available to assess the functional properties of the trabecular tissue—properties that are necessary to maintain IOP in a narrow range.^{31,32} A more robust technique to assess the functionality

[#]Authors contributed equally to this work.

Address all correspondence to: Ruikang K. Wang, University of Washington, Bioengineering & Ophthalmology, Box 355061, 3720 15th Avenue NE, Seattle, Washington 98195-5061. Tel: (206) 616-5025; Fax: (206) 685-3300; E-mail: wangrk@uw.edu

of the tissues controlling IOP could enable early diagnosis and treatment for those at risk, reducing reliance on progressive visual system damage as a guide for management.

IOP is regarded as the major risk factor and the only treatable problem in glaucoma.² The aqueous outflow system (AOS), the pathway for aqueous humor to leave the eye, involves passage of aqueous from the trabecular meshwork (TM) into the Schlemm's canal (SC), and then into the collector channels (CCs). From the CCs, the aqueous enters the aqueous veins and then the episcleral veins. A recent model of the AOS indicates that the TM acts as a biomechanical pump, which induces pulsatile flow.³³⁻³⁶ Failure of the pulsatile flow mechanism results in an increase of outflow resistance. Clinical and laboratory evidence³³⁻³⁶ points to alterations in elasticity and compliance as changes responsible for increased outflow resistance in glaucoma patients. Current acceptance of the TM as the source of resistance is illustrated by the recent use of stents to bypass abnormal trabecular tissues in an attempt to re-establish normal rates of aqueous flow into the SC.^{37,38}

A body of evidence indicates that the aqueous outflow from the SC is pulsatile and synchronous with IOP transients.^{33,34,39-41} Transients such as the cardiac pulse cannot transfer pressure gradients directly from the anterior chamber to SC because of the complex labyrinthine structure of the TM. An explanation for the pulsatile flow in the SC may be due to the trabecular tissue movement in response to the cardiac pulse. However, no technologies have thus far identified such movement, probably because the TM is located deep within the corneo-scleral limbus, and its movement is too small (in the micron range) to be detected by any currently available technologies, either *in vivo* or *in vitro*. The current report meets this challenge by describing a noninvasive, yet highly sensitive method that is capable of characterizing TM movement in response to an experimentally induced ocular pulse in an *ex vivo* primate model.

OCT is a powerful noninvasive, noncontact, three-dimensional (3-D), real-time imaging modality with high spatial resolution ($\sim 10 \mu\text{m}$ axially).^{10,42-45} Studies have revealed the potential of using an anterior segment OCT to image the AOS^{38,44,46-51} and to visualize the TM and the SC,⁴⁴ with their appearances in the OCT images confirmed by histological correlations.⁴⁶ A recent report proposed the use of a polarization-sensitive OCT to image the AOS with an enhanced ability to visualize the TM.⁴⁷ By integration with a prototype endoscopic probe, OCT has also been reported to guide implantation of stents during SC surgery³⁷ and to identify the CCs in human cadaver eyes.³⁸

Due to its high resolution ($\sim 10 \mu\text{m}$) and high imaging speed ($\sim 100\text{-kHz}$ line rate), it is now possible for OCT to provide quantifiable *in vivo* information about tissue structures with a size comparable with or greater than the OCT resolution. For example, a number of recent studies have reported the use of real-time OCT to quantify the geometrical sizes of the TM³⁰ and SC^{46,48,49} as well as to map the surrounding microcirculation of the AOS.^{50,51} Regional differences of SC size^{48,49} as well as differences between normal and glaucomatous subjects⁴⁸ have been explored. Furthermore, several methods have been developed to measure fundus pulsations using OCT⁵² or low-coherence interferometry.^{53,54} Notwithstanding, all these studies are based on OCT microstructural images to identify and track structural boundary positions (e.g. cornea and retina), which are, however, not feasible for measuring TM movement. This is because 1) the visibility of the TM boundary is often poor,

and 2) the amount of TM movement is typically $\leq 2 \mu\text{m}$, which is beyond the limits of resolution attainable with OCT structural measurements.

To measure such small tissue movement, one has to use the phase information embedded in OCT signals, rather than the amplitude information that is often used to reconstruct the OCT images. This is because the change of optical phase is much more sensitive to tissue movement than that of amplitude. This concept was first reported in 2006⁵⁵ where the phase changes between adjacent A-scans were used to measure the tissue movement, also called tissue Doppler OCT (tDOCT), a method similar to that of phase resolved OCT to measure blood flow.⁵⁶ It was then quickly realized that the phase noise from such treatment is high due to the heterogeneous properties of the biological tissue, which causes deterioration of the spatial correlation between the adjacent A-scans.⁵⁷ In addition, the time interval, τ , between the adjacent A-scans in real time OCT systems is short (in the microsecond range), making the measurement of slow tissue movement difficult. These factors combined prevent the tDOCT from measuring small tissue movements less than $1 \mu\text{m}$.⁵⁸ To mitigate this problem, a phase sensitive OCT (PhS-OCT) was developed in 2007 that uses the phase changes between adjacent B-scans to measure the tissue movement.⁵⁸ The report demonstrated that PhS-OCT is extremely sensitive to tissue motion as small as 0.26 nm , a sensitivity made possible by the much increased time interval τ which is typically several hundred times that of tDOCT.

In this pilot study, we report for the first time the use of PhS-OCT to image/visualize TM movement with sensitivity at the nanometer scale. We used nonhuman primate eyes for this proof of concept. To achieve our objectives, we designed an anterior segment perfusion system that is capable of providing sinusoidal IOP transients, thus permitting the primate eyes to mimic the *in vivo* ocular pulse generated by the cardiac cycle. A real-time PhS-OCT system working at 92-kHz line rate was used to image the AOS of the primate eyes in response to experimentally induced IOP transients, enabling quantitative assessment of dynamic TM movement *in situ*.

2 Materials and Methods

2.1 System Setup and Methodology

The schematic of the experimental setup used to image/measure dynamic TM movements in response to IOP transients is shown in Fig. 1. The setup consists primarily of three units: a PhS-OCT system to image the AOS, a perfusion system to control the IOP, and a controlling unit to provide synchronization during data acquisition.

The PhS-OCT system (Fig. 1) used in this study is based on a spectral domain OCT (SD-OCT) configuration, in which a broadband superluminescent diode with a central wavelength of 1340 nm and a spectral bandwidth of 110 nm is used to achieve a high axial resolution (theoretically $\sim 7.2 \mu\text{m}$ in air). In the sample arm, an objective lens (focal length 50 mm) is used to focus the probing light on the region of interest (ROI), i.e. the corneo-scleral limbus, yielding a measured lateral resolution of $\sim 16 \mu\text{m}$. The spectrometer is equipped with an InGaAs line scan camera capable of $\sim 92\text{-kHz}$ A-line scan rate. The spectrometer has a spectral resolution of 0.14 nm providing a measured imaging depth of $\sim 3.0 \text{ mm}$ in air. The system dynamic range was measured at $\sim 105 \text{ dB}$ at the depth-position

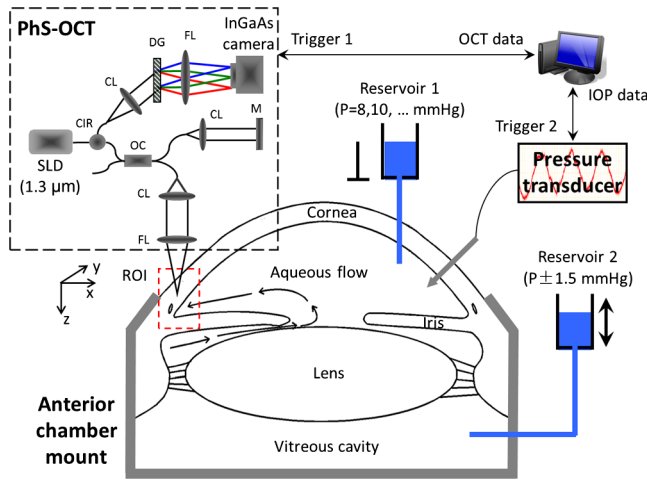


Fig. 1 Schematic diagram of the experimental setup for imaging the anterior segment (PhS-OCT) and controlling IOP within the anterior chamber. Reservoir 1 establishes a mean IOP in the anterior chamber of the eye; Reservoir 2 establishes a mean IOP in the posterior chamber of the eye and induces a sinusoidal IOP gradient change with a peak-to-peak amplitude of 3 mmHg at 1 pulse/second. A pressure transducer records IOP in real time; Trigger 1 triggers PhS-OCT for imaging; Trigger 2 triggers pressure transducer for recording. ROI indicates the OCT imaging area. OC: optical coupler; CIR: circulator; CL: collimating lens; FL: focusing lens; M: mirror; OL: objective lens; DG: diffraction grating.

of 0.5 mm with an incident optical power of 2.5 mW in the sample arm.

Four *ex vivo* monkey eyes (nemestrina), having an outflow system similar to humans, were used in this study. The enucleated eyes were obtained from the University of Washington Primate Center and harvested within ~ 0.5 h of initiation of the experiments. A system for imaging the anterior segment by PhS-OCT was designed by mounting the eye in a device that encompassed a region about 6-mm posterior to the limbus (see Fig. 1). Since the mean IOP *in vivo* is ~ 16 mmHg and the mean episcleral venous pressure is ~ 8 mmHg, the pressure differential between the anterior chamber and episcleral vein under normal conditions is ~ 8 mmHg. Because *ex vivo* eyes do not have episcleral venous pressure, an IOP of 8 mmHg was used to approximate the pressure gradient present *in vivo*. To control the IOP, the height of two reservoirs leading to the anterior chamber (reservoir 1) and posterior chamber (reservoir 2) were adjusted. An anterior chamber needle connected to a pressure transducer (PowerLab, ML866) was used to continuously monitor the anterior chamber mean IOP and pulse amplitudes. Reservoir 2 was used to induce sinusoidal IOP transients that mimic the ocular pulse, with a peak-to-peak amplitude of 3mmHg and a frequency of 1 pulse/second. Two trigger signals (trigger 1 to the OCT imaging system; trigger 2 to the pressure transducer) were generated by a computer to synchronize the data acquisition of the PhS-OCT system and the pressure transducer. Repeated OCT B-frames (MB-mode scan) were acquired at the same location at the limbal region of the anterior chamber (as indicated by ROI in Fig. 1). Each B-frame containing 512 A-lines and 500 repeated B-frames was acquired with a frame rate of ~ 140 fps, during ~ 3.5 s of IOP pulse transients. The experiments were replicated at seven graded mean IOPs (IOP = 5, 8, 10, 20, 30, 40, 50 mmHg).

In spectral domain OCT, the interference signal between the reference and the scattering light from within a sample is spectrally resolved by a linear array detector (InGaAs camera in Fig. 1). By ignoring the terms that do not contribute to the OCT image formation, the OCT signal that localizes the scatter within a sample over a B scan at time instant t can be expressed as

$$f(x, z, t) = A(x, z, t) \exp[-i\phi(x, z, t)], \quad (1)$$

where (x, z) denotes the lateral and depth coordinates of the scatter position within the cross-section (B-scan) OCT image. Equation (1) is a complex function where the amplitude, $A(x, z, t)$ is used to generate the traditional OCT structural images, whereas the phase term $\phi(x, z, t)$ generally random, but fixed for the static scatter at the position (x, z) . However, if the scatter moves by an instantaneous distance $\Delta d(x, z)$ ring a time interval τ between two successive B scans, a localized change in the measured phase of the reflected light will be induced, which is given by

$$\Delta\phi(x, z, t) = \frac{4\pi\Delta d(x, z, t)}{\lambda_0}, \quad (2)$$

where λ_0 is the central wavelength of the light source, and n is the refractive index of the sample which is typically 1.38 for most soft tissues.⁵⁹ In this study, the phase-frame $\Delta\phi(x, z, t)$ as initially measured by calculating the phase shift between the successive B-frames, and then every fivephase-frames were averaged to minimize the effect of phase noise on the final results. Thus the localized tissue velocity in the beam direction can be deduced,

$$v(x, z, t) = \frac{\Delta\phi(x, z, t)\lambda_0}{4\pi n\tau}. \quad (3)$$

For limited tissue motion, the correlation between the phase measurements of successive B scans is well preserved because the M-B mode of scanning is used in this study. Note that because the imaging speed of the system was 140 fps, the time interval was $\tau = 7.1$ ms in this study. After the depth-resolved instantaneous displacement and velocity are derived, the amount of tissue movement over a time period of T can be obtained by integrating Eq. (3) over the time variable,

$$d(x, z) = \int_0^T \frac{\Delta\phi(x, z, t)\lambda_0}{4\pi n\tau} dt. \quad (4)$$

With these dynamic parameters, the strain rate $\epsilon(x, z, t)$ can be calculated to quantify the local response of the tissue, such as the TM, to the IOP transients as follows,

$$\epsilon(x, z, t) = \frac{dv(x, z, t)}{dz}. \quad (5)$$

Alternatively, the strain rate can be evaluated by taking the slope of the velocity curve along the vertical axis (probe beam direction), which was the method used in this study. To improve the accuracy, we used a linear fitting algorithm reported in Ref. 60 to estimate the slope of the TM velocity curve.

It is known that the OCT phase measurement described above is only sensitive to tissue movement along the probe beam direction. In other words, the true tissue movement can be obtained only if the Doppler angle is known *a priori*. It should be noted that the TM is oriented circumferentially around the anterior segment, while the OCT imaging is performed radially in this study. Thus the TM surface is orthogonal to the scanning plane i.e. the B-frames and the pressure and velocity direction is perpendicular to the TM surface. As illustrated in Fig. 2, it is trivial to find that the Doppler angle, α , can be calculated as the angle between the TM surface and the horizontal plane (x - y plane). With this Doppler angle, the tissue velocity, movement and strain rate as described in Eq. (3) through

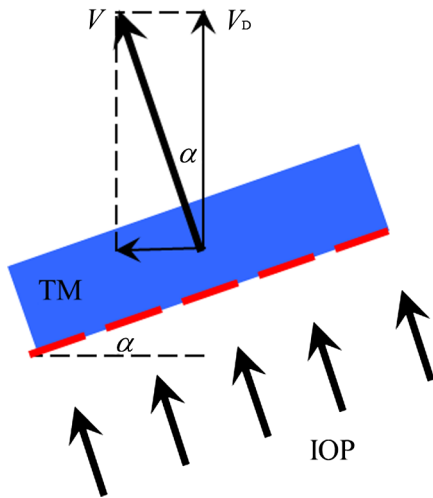


Fig. 2 Schematic diagram of Doppler angle correction.

Eq. (5), respectively, are modified by dividing the measured values by $\cos(\alpha)$ to provide their true values.

2.2 Theoretical Considerations

According to the pulsatile flow model,³³⁻³⁶ the increase in the IOP transients, due to the ocular pulse, blinking, and eye movement, displaces the SC endothelium (SCE) outward into the SC, placing the TM under tension. Outward TM movement narrows the SC, which as a result discharges the aqueous from the SC into the CCs and the aqueous veins. Concurrently, the TM stretches, allowing the aqueous in the anterior chamber to pass through the TM interstices and enter one-way aqueous valves. During the decrease of the IOP transient, the TM recoils, leading to a pressure reduction in the SC and the aqueous to flow from the aqueous valves into the SC.

It is useful to theoretically estimate the TM movement with each pulse wave to fully account for aqueous outflow in the primate eyes. To simplify the calculation, the elongated lumen SC oriented circumferentially around the anterior segment may be modeled as a rectangular box, with length (L) × width (W) × height (H), as illustrated in Fig. 3. Corneal diameter near the corneo-scleral junction is ~9.5 mm⁶¹ from which we estimate the SC diameter to be about 1 mm larger (~10.5 mm). Using a 10.5 mm diameter, the circumference of the SC is determined to be ~33 mm [refer to Fig. 3(a)], which is used as the length (L) of the rectangular box in our model. The anterior-posterior length of SC has been measured to be 230 to 30 μm,⁶¹ which is used as the width (W) of the rectangular box [refer to Fig. 3(b)]. The total height of the box is estimated to be 11 μm.⁶¹

Aqueous flow has been estimated to be 1.5 μl/min.^{62,63} For a 60-beats-per-minute heart rate, the aqueous stroke volume with

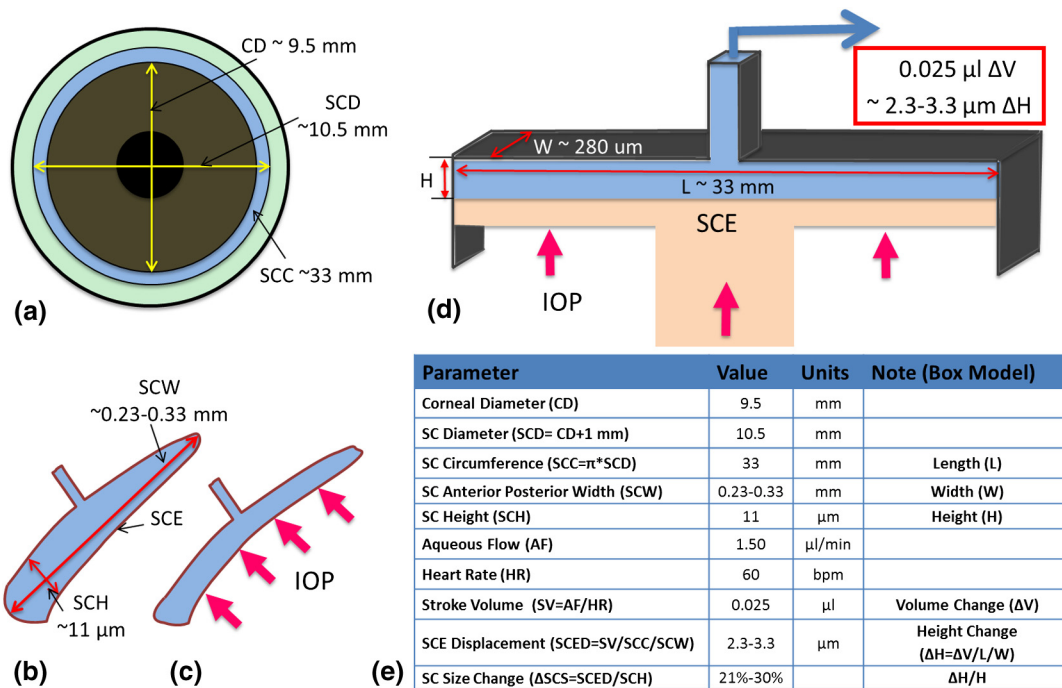


Fig. 3 SC Deformation Model. (a) Schematic diagram of the front view of the eye. (b) Schematic diagram of the SC cross-section and (c) outward displacement of the SCE into the SC induced by an increase of IOP transient. (d) Schematic diagram of the rectangular box model that approximates the change in the SC volume. (e) Table summarizing the parameters and equations used in the theoretical estimation of the SCE movement.

each pulse wave, which corresponds to the change in SC volume (ΔV) per heartbeat, is therefore $0.025 \mu\text{l}$. To cause a $0.025 \mu\text{l}$ change in the SC volume, a change in the height of the rectangular box (ΔH) should then be ~ 2.3 to $3.3 \mu\text{m}$ [refer to Fig. 3(c) and 3(d)]. According to the pulsatile flow model, the change in the box height (ΔH) can be considered as a % change of SCE moving into SC, i.e., $\Delta H/H \times 100$ or $\sim 21\%$ – 30% . During one aqueous pulse wave, the SC size change (ΔSCS) should also be $\sim 21\%$ to 30% . The calculations have been summarized in Fig. 3(e).

3 Results

Figure 4(a) is a schematic representation of structural relationships and pathways of the AOS. Aqueous humor, which is generated by the ciliary processes, travels from the posterior to the anterior chamber of the eye through the pupil, and exits the eye via the aqueous outflow pathway which is located at the corneo-scleral limbus and includes the TM, SC, CCs, and aqueous and episcleral veins.^{33–36} The AOS structural elements are summarized in Fig. 4(b). The dashed square marked in Fig. 4(a) indicates the area for PhS-OCT imaging. Figure 4(c) is a representative OCT image captured from an enucleated nonhuman primate eye, where the important structural features such as the TM, SC and CC can be clearly identified. However, due to the limited imaging resolution of the system ($\sim 7 \mu\text{m}$ axial and $16 \mu\text{m}$ lateral), it is difficult to visualize/measure the small movement of the TM induced by the IOP transients.

The potential of PhS-OCT to visualize/image the dynamic movement of the AOS, particularly the TM, is demonstrated in Fig. 5. With the mean IOP maintained at 8mmHg, the pulse amplitude of 3 mmHg and the pulse rate kept at 1 pulse/second,

the typical tissue velocity maps of the scanned cross-section are given in Fig. 5(a) and 5(b) captured at the systolic (maximum) and diastolic (minimum) phases, respectively. The images demonstrate that the TM moves outward into the SC during systole [Fig. 5(a)], while it moves inward away from SC during diastole [Fig. 5(b)]. Figure 5(c) and 5(d) present the depth-dependent velocity profiles along the vertical dashed lines in Fig. 5(a) and 5(b). The largest movement is located in the area closest to SCE. The slopes of the TM velocity versus depth are marked by the thick lines in Fig. 5(c) and 5(d) and are considered to represent the strain rate of the corresponding tissue; i.e., the TM deformation speed, which was almost linear.

In the corresponding microstructural OCT images, SC appeared as a low-intensity area adjacent to the TM [Fig. 5(e) and 5(f)]. Given the resolution of the current system, the measurement of the SC area within the scanned cross-section is feasible. We therefore segmented the boundary of the SC lumen, as shown in Fig. 5(g). A schematic diagram of the SCE attachment to the underlying trabecular lamellae is depicted in Fig. 5(h). SCE connects with the juxtacanalicular cells, which in turn attach to the trabecular lamellae via the cytoplasmic cell processes.^{33,34}

After localizing the TM and SC in the structural OCT images (e.g., Fig. 5), the time-lapse parameters of the TM velocity, displacement, and strain rate can be obtained by the use of Eq. (3) through Eq. (5) described in Sec. 2. These parameters are important for a detailed investigation of the dynamic pulse-dependent TM behavior. Figure 6 demonstrates such a result, displaying the temporal relationship of the induced IOP pulsations [Fig. 6(a)] to the TM velocity [Fig. 6(b)], displacement [Fig. 6(c)], and strain rate [Fig. 6(d)] obtained from one eye.

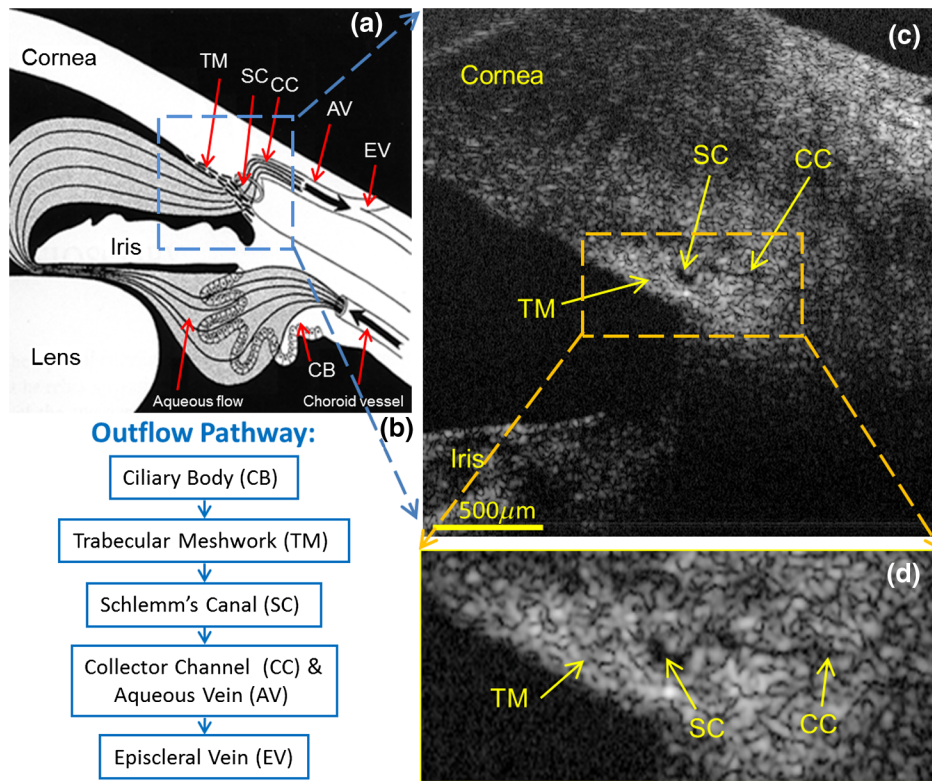


Fig. 4 PhS-OCT is capable of imaging important microstructural features of the AOS. (a) and (b) Schematic diagram and flow chart of the aqueous outflow pathway, respectively; (c) are presentative OCT microstructural cross-section of the corneo-scleral limbus [marked by the dashed blue square in (a)]; (d) enlarged view of the area marked by the dashed yellow square in (c). The schematic of (a) is modified from Refs. 33 and 34.

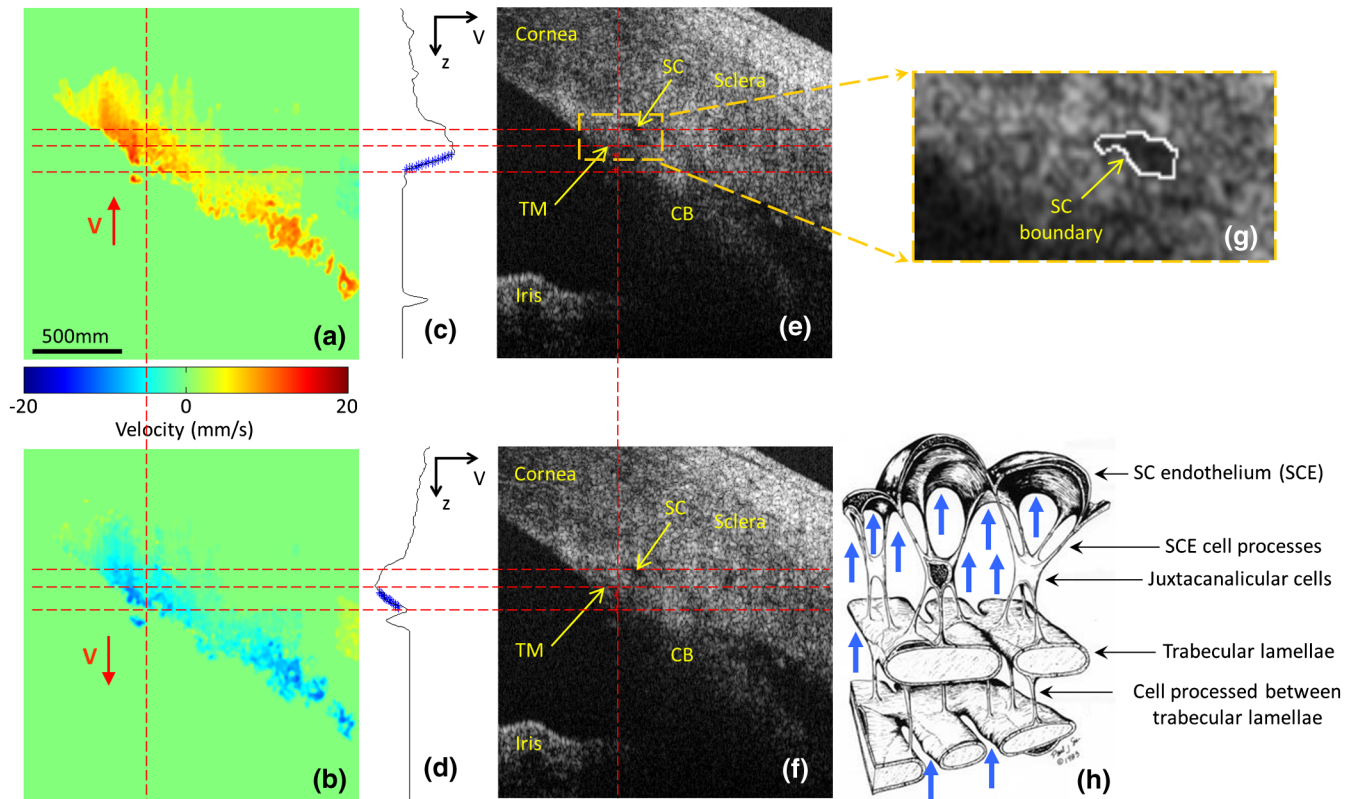


Fig. 5 *Ex vivo* pulse-induced TM movement and SC deformation in nonhuman primate eye at 8 mmHg mean IOP. Representative cross-sectional images of tissue velocity in the corneo-scleral limbus: (a) red corresponds to TM movement into SC during systole; (b) blue corresponds to TM movement away from SC during diastole; (c) and (d) depth-dependent velocity profiles along the vertical dashed lines in (a) and (b), respectively; (e) and (f) Corresponding OCT microstructural images from (a) and (b). (g) Enlarged view of the area marked by the dashed yellow square in (e). The closed white curve in (g) depicts the boundary of the SC. (h) Schematic of the SC endothelial attachment to the underlying trabecular lamellae (adopted from Refs. 33 and 34). The bold arrows in (H) indicate tissue responses to deforming forces induced by IOP transients. The horizontal lines are used to mark approximately the position of TM, facilitating comparison between figures given.

In Fig. 6(e) the changes of SC size normalized to the maximal SC dimension at the corresponding mean IOP level are shown. These results were obtained under the following conditions: 8-mmHg mean IOP, 3-mmHg IOP pulse amplitude, and 1 pulse/second. The oscillations in TM displacement and SC size were synchronous with the IOP pulse wave, but involved a phase delay. The trough of the SC size curve came immediately after the IOP pulse peak, while the peak of the TM displacement came later than the trough of the SC size curve.

At the different mean IOP levels of 8, 10, and 40 mmHg, structural SC cross-sections (obtained at the same spatial position and at the same phase of the IOP pulse wave) are shown along with the corresponding TM movement in Fig. 7. In the experiments, a pulse amplitude of 3 mm Hg and frequency of 1 pulse/second were induced at each mean IOP level. The images demonstrate that the increase of mean IOP was associated with progressive TM distention into SC, leading to TM apposition to SC external wall [comparing Fig. 7(a) and 7(b) with 7(c) acquired at the same phase of IOP transient], and was associated with the decrease of TM movement [Fig. 7(d) to 7(f)]. Calculations of IOP-dependent SC size changes (Δ SCS) were consistent with findings from the OCT images (see Fig. 8 for quantitative results).

Normalized mean SC size and peak-to-peak TM displacement (ppTMD) in response to a 3-mm pulse amplitude were quantified while maintaining mean IOPs of 5, 8, 10, 20, 30, 40, and 50 mmHg, respectively. Results are summarized in

Figs. 8 and 9, respectively. Both the mSCA and the ppTMD decreased exponentially as the mean IOP increased. The standard deviation for TM displacement decreased as the mean IOP increased. At 8 mmHg mean IOP, the peak-to-peak SC size change (Δ SCS) was $\sim 30\%$ of the maximal SC dimension and the ppTMD was $\sim 2.28 \mu\text{m}$ during one IOP transient.

4 Discussion

The PhS-OCT technique described in this report provides quantitative *ex vivo* evidence of synchronous TM displacement in response to IOP transients that simulate the normal *in vivo* ocular pulse. The *ex vivo* model enables the study of the pulse-induced TM displacement while simultaneously providing the ability to correlate TM displacement changes with SC dimension changes.

Ideally, laboratory studies exploring IOP regulatory mechanisms should provide insights directly translatable to improved glaucoma management. One study limitation is the use of a non-human primate model that may not fully reflect behavior in the human eye. However, anatomic features are remarkably similar to the human eye.³³ A second limitation is the lack of normal episcleral venous pressure or afterload.⁵¹ An attempt has been made to minimize the problem by choosing pressure gradients that are reflective of the normal pressure difference experienced in the outflow system. A related limitation is the absence of normal ciliary body tone that provides tensioning of the scleral spur and TM *in vivo*. In addition, the resolution of the OCT system is

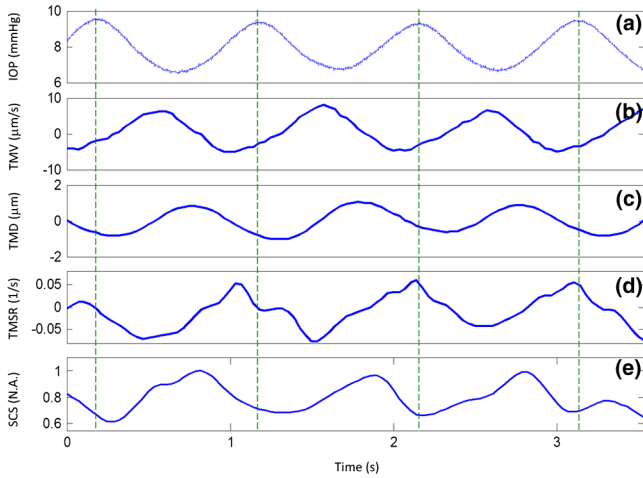


Fig. 6 (a) Temporal plots over 3.5 s of IOP measurements provided by the in-line pressure transducer, (b) trabecular meshwork velocity (TMV); (c) trabecular meshwork displacement (TMD); (d) trabecular meshwork strain rate (TMSR) and (e) normalized SC size (SCS). The experimental conditions were mean IOP 8 mmHg, pulse amplitude 3 mmHg and 1 pulse/second. The dashed vertical lines indicate the time of the IOP pulse peaks.

not sufficient to study structural elements in SC that appear to subservise a valve-like function.³³ However, the measurement of TM displacement and visualization of SC dimension changes in this study provide a useful mean to correlate pulse-dependent outflow system behavior and global SC size changes.

Displacement of the TM structural elements detected by PhS-OCT varied regionally within the TM tissue. Displacement of the TM tissue elements seemed greater in the regions closer to

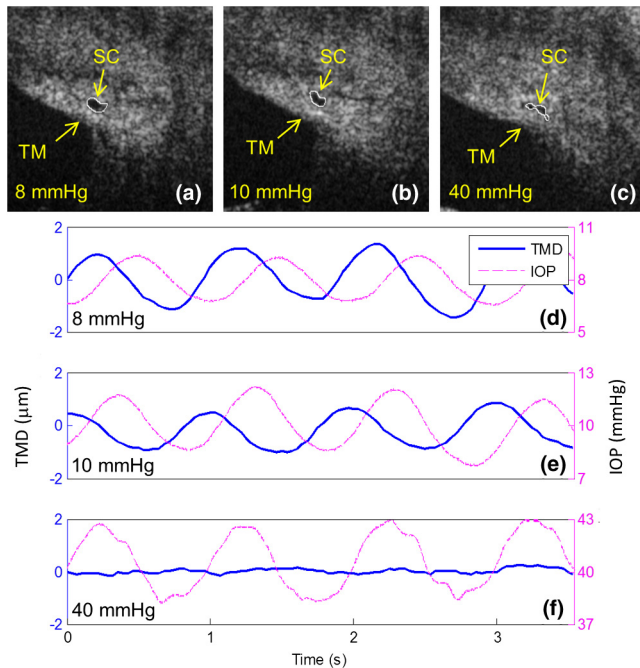


Fig. 7 IOP-dependence of SC deformation and TM movement. (a) to (c) Images of the same SC cross-sections at an IOP of 8, 10, and 40 mmHg, respectively, (d) to (f) corresponding plots of TM displacement versus time. While the IOP transients (dashed lines) are relatively unchanging at three mean IOP levels, the ability of TM movement (solid lines) is markedly reduced with the increase of the mean IOP level.

the endothelium lining of the SC, and progressively diminishing in the tissues closer to the anterior chamber, as shown in Fig. 5(c) and 5(d). Histological evidence is consistent with the finding from PhS-OCT. The entire monolayer of the endothelium lining distends outward into the SC in response to the IOP-induced forces, with the distention being limited by extensive tethering of endothelium to the trabecular lamellae.^{33,34} As a result, the greatest TM distention occurs in the region closest to the epithelial layer of the SC as shown in Fig. 5(h).^{33,34}

The IOP pulse peak could be expected to correspond to the peak of the TM displacement at which time the dimension of the SC becomes the smallest (i.e., trough in the curve). Figure 6 demonstrates that, after the IOP pulse peak, the trough of SC curve came earlier than the peak of TM velocity and TM displacement. The delay most likely suggests that the force of IOP transients affects the endothelium layer earlier than the trabecular lamellae, which are the elements primarily measured by PhS-OCT, due to their larger size. The delay in responses between the SC and the TM is consistent with the pressure dependent endothelium displacement occurring first followed by force transmission to the trabecular beams through the tethering mechanism observed histologically.^{64,65}

As the mean IOP increases (refer to Figs. 8 and 9), the ability of TM and SC to respond to the IOP transients decreases. One explanation for the reduced ability of TM to move may be the apposition between the TM and SC external wall [refer to Figs. 7(a) to 7(c) and 8]. Apposition of SC walls was correlated with a reduction in TM displacement in this study [refer to Figs. 7(d) to 7(f) and 9]. Reduced TM excursions in response to the ocular pulse as IOP increases will necessarily reduce the amount of aqueous that can be discharged with each transient pulse wave, thus leading to a further increase in mean IOP and potentially introducing a deleterious feedback loop.

At 8 mmHg corresponding to a physiologic pressure gradient, the measured values of the peak-to-peak change of the SC dimension and the peak-to-peak movement of TM are $\sim 30\%$ and $\sim 2.27 \mu\text{m}$, respectively, which are values close to the theoretical estimates of $\sim 21\%$ to 30% and ~ 2.3 to $3.3 \mu\text{m}$ (see Sec. 2.2). The standard deviation of the measured movement of

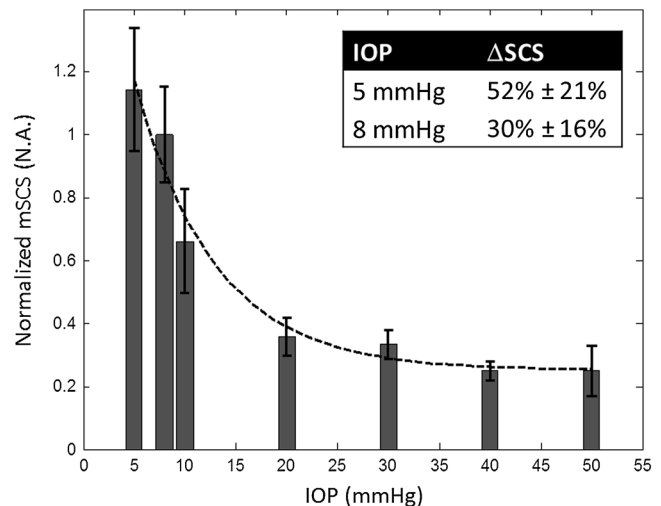


Fig. 8 Mean and standard deviation of the normalized mean SC dimension as a function of the mean IOP. The data was fit to an exponential curve. The inserted table lists the peak-to-peak SC size change (ΔSCS) at 5 and 8 mmHg mean IOPs (each mean IOP has two values).

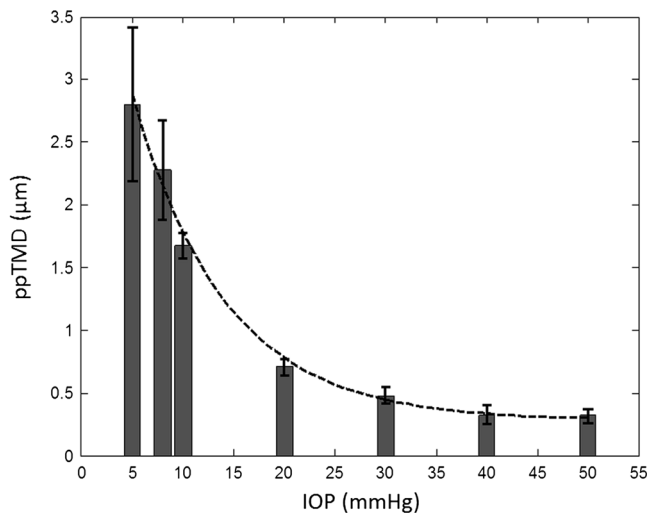


Fig. 9 Mean and standard deviation of the ppTMD as a function of the mean IOP. The data was fit to an exponential curve.

the TM was larger at lower mean IOPs, which may be due to the higher elasticity of the tissue at lower pressures.

Changes in the SC dimensions were quantified based on the segmentation of the structural images with a resolution of ~ 1 pixel (~ 4 to $5 \mu\text{m}$). This limits its quantification for higher mean IOPs where the changes in the size of the SC are small. This resolution limitation permitted obtaining two values for the measurement of the changes in SC dimension only at the mean IOPs of 5 and 8 mmHg. In contrast, quantification of TM displacement by the PhS-OCT method described in this paper is capable of submicron resolution.

The highly sensitive measurement of the TM movement afforded by a relatively low spatial resolution PhS-OCT system resulted in a large available dynamic range with the resultant ability to detect submicron TM movement. Such high sensitivity offers the potential to make PhS-OCT an effective screening tool for identifying patients at risk for IOP elevation in glaucoma. More importantly, the dynamic range offers the possibility of developing a sensitive, objective technique for identifying progressive TM functional abnormalities associated with the loss of the ability to maintain IOP within a normal range.

This PhS-OCT study documents a reduction in the magnitude of TM movement in response to an increase of the mean IOP (refer to Figs. 7 and 9). *Ex vivo* experimental counterparts³⁴ include evidence that the TM progressively distends into the SC, and eventually resting against SC external wall as the mean IOP increases.³³ Apposition of the walls of the SC necessarily leads to progressive limitation of the TM displacements. A corresponding increase in resistance due to aqueous outflow is well documented.³⁴ *In vivo* counterparts include evidence that the incidence of visible pulsatile aqueous outflow decreases as the mean IOP increases; visible pulsatile flow is generally absent at an IOP above ~ 28 mmHg.³⁶

In vivo evidence is also consistent with a loss of TM compliance and elasticity in glaucoma.³⁴ Pressure reversal studies during gonioscopy have documented that blood rapidly enters and fills the SC and leaves when normal gradients are restored in subjects without glaucoma. As the glaucoma process develops, entry and exit of blood into the SC slows down, eventually leading to only patchy filling of the canal with blood. In advanced diseases, blood does not enter the SC. Investigators

have concluded that as glaucoma progresses, the trabecular tissues gradually stiffen, preventing rapid movement of blood into and out of SC with TM tissues eventually in permanent contact with SC external wall completely preventing blood reflux.³⁴

The TM displacement documented in this study results from movement that is determined by compliance and elasticity of the TM tissue. Such tissue properties in turn determine the functional behavior of the TM, properties that also may be reasonably expected to play an important role in maintaining normal IOP homeostasis. The sensitivity of PhS-OCT to tissue movement provides a large dynamic range, offering the potential for a technique capable of monitoring the functional properties of the outflow system *in vivo*.

A sensitive objective noninvasive test that characterizes IOP regulatory mechanisms may improve the diagnosis and treatment of glaucoma. Although office-based tonometry is a useful technique, it is dependent on corneal properties that often lead to measurement errors.⁶⁶⁻⁶⁹ Furthermore, testing only involves brief measurements four times a year and the measurements do not adequately reflect diurnal and longer-term IOP variability.

In the treatment of glaucoma, some widely used glaucoma medications, such as prostaglandins and adrenergics, are found to increase aqueous outflow by increasing pulsatile flow from the SC into the aqueous veins, a response that occurs within minutes of instillation. The increases in pulsatile flow from the SC should increase the TM displacement. Using PhS-OCT, medication nonresponders might be rapidly identified through monitoring of medication-dependent alterations of the TM displacement. By identifying nonresponders, patients would be spared the cost and inconvenience of what for them is an ineffective medication.

Current study used the proposed PhS-OCT system to track small TM motion in the enucleated primate monkey eyes beyond the imaging system resolution. Challenges ahead will be to translate this technique to image *in vivo* human eyes, where bulk tissue motion, other than that of the TM, is inevitable. Active research is currently underway to develop motion-compensation algorithms; for example, using speckle tracking and/or phase-resolved Doppler approaches^{70,71} in order to minimize/eliminate the bulk tissue movement due to involuntary subject movement.

5 Conclusion

This study describes a new sensitive PhS-OCT method to assess pulse-dependent TM movement in an *ex vivo* primate model system, with an ability to measure the small tissue movement beyond its structural imaging resolution. The technique provides quantitative evidence of synchronous TM displacement in response to IOP transients that simulate the normal *in vivo* ocular pulse. In this model system, the pulse-induced TM displacement was dependent on mean IOP; as IOP increased, the TM displacement decreased markedly. At the same time, the quantitative measurement of SC demonstrated a corresponding marked reduction in the SC dimension.

Evidence of TM movement obtained with the PhS-OCT technique is consistent with findings from histological and clinical studies. Such studies indicate that the trabecular tissue elasticity and compliance are the properties important for IOP regulation, the only treatable problem in glaucoma. Since PhS-OCT is a highly sensitive technique to assess functional properties associated with TM movement, the technique may

provide new information to aid decision making in glaucoma management.

Acknowledgments

This research was supported in part by an Innovative Ophthalmic Research Award from Research to Prevent Blindness.

References

- H. A. Quigley and A. T. Broman, "The number of people with glaucoma worldwide in 2010 and 2020," *Br. J. Ophthalmol.* **90**(3), 262–267 (2006).
- American Academy of Ophthalmology Glaucoma Panel. Preferred Practice Pattern® Guidelines. Primary Open-Angle Glaucoma. San Francisco, CA: American Academy of Ophthalmology; 2010. Available at: www.aao.org/ppp.
- M. G. Hattenhauer et al., "The probability of blindness from open-angle glaucoma," *Ophthalmology* **105**(11), 2099–2104 (1998).
- Y. H. Kwon et al., "Rate of visual field loss and long-term visual outcome in primary open-angle glaucoma," *Am. J. Ophthalmol.* **132**(1), 47–56 (2001).
- J. S. Schuman et al., "Quantification of nerve fiber layer thickness in normal and glaucomatous eyes using optical coherence tomography," *Arch. Ophthalmol.* **113**(5), 586–596 (1995).
- B. Cense et al., "Thickness and birefringence of healthy retinal nerve fiber layer tissue measured with polarization-sensitive optical coherence tomography," *Invest. Ophthalmol. Vis. Sci.* **45**(8), 2606–2612 (2004).
- F. A. Medeiros et al., "Evaluation of retinal nerve fiber layer, optic nerve head, and macular thickness measurements for glaucoma detection using optical coherence tomography," *Am. J. Ophthalmol.* **139**(1), 44–55 (2005).
- J. E. DeLeon Ortega et al., "Effect of glaucomatous damage on repeatability of confocal scanning laser ophthalmoscope, scanning laser polarimetry, and optical coherence tomography," *Invest. Ophthalmol. Vis. Sci.* **48**(3), 1156–1163 (2007).
- B. Povazay et al., "Minimum distance mapping using three-dimensional optical coherence tomography for glaucoma diagnosis," *J. Biomed. Opt.* **12**(4), 041204 (2007).
- T. Mumcuoglu et al., "Improved visualization of glaucomatous retinal damage using high-speed ultrahigh-resolution optical coherence tomography," *Ophthalmology* **115**(5), 782–789 (2008).
- M. Yamanari et al., "Phase retardation measurement of retinal nerve fiber layer by polarization-sensitive spectral-domain optical coherence tomography and scanning laser polarimetry," *J. Biomed. Opt.* **13**(1), 014013 (2008).
- M. Pircher, C. K. Hitzenberger, and U. Schmidt-Erfurth, "Polarization sensitive optical coherence tomography in the human eye," *Prog. Retin. Eye Res.* **30**(6), 431–451 (2011).
- T. Shoji et al., "Assessment of glaucomatous changes in subjects with high myopia using spectral domain optical coherence tomography," *Invest. Ophthalmol. Vis. Sci.* **52**(2), 1098–1102 (2011).
- N. G. Strouthidis et al., "Longitudinal change detected by spectral domain optical coherence tomography in the optic nerve head and peripapillary retina in experimental glaucoma," *Invest. Ophthalmol. Vis. Sci.* **52**(3), 1206–1219 (2011).
- R. N. Weinreb, S. Shakiba, and L. Zangwill, "Scanning laser polarimetry to measure the nerve fiber layer of normal and glaucomatous eyes," *Am. J. Ophthalmol.* **119**(5), 627–636 (1995).
- N. T. Choplin et al., "Retinal nerve fiber layer measurements do not change after LASIK for high myopia as measured by scanning laser polarimetry with custom compensation," *Ophthalmology* **112**(1), 92–97 (2005).
- N. T. Choplin, Q. Zhou, and R. W. Knighton, "Effect of individualized compensation for anterior segment birefringence on retinal nerve fiber layer assessments as determined by scanning laser polarimetry," *Ophthalmology* **110**(4), 719–725 (2003).
- W. V. Hatch et al., "Laser scanning tomography of the optic nerve head in ocular hypertension and glaucoma," *Br. J. Ophthalmol.* **81**(10), 871–876 (1997).
- S. Melamed and H. Levkovich-Verbin, "Laser scanning tomography and angiography of the optic nerve head for the diagnosis and follow-up of glaucoma," *Curr. Opin. Ophthalmol.* **8**(2), 7–12 (1997).
- J. C. Tan and R. A. Hitchings, "Approach for identifying glaucomatous optic nerve progression by scanning laser tomography," *Invest. Ophthalmol. Vis. Sci.* **44**(6), 2621–2626 (2003).
- M. B. Wax et al., "Emerging perspectives in glaucoma: optimizing 24-h control of intraocular pressure," *Am. J. Ophthalmol.* **133**(6), S1–S10 (2002).
- D. J. Coleman and S. Trokel, "Direct-recorded intraocular pressure variations in a human subject," *Arch. Ophthalmol.* **82**(5), 637–640 (1969).
- S. Mosaed, J. H. Liu, and R. N. Weinreb, "Correlation between office and peak nocturnal intraocular pressures in healthy subjects and glaucoma patients," *Am. J. Ophthalmol.* **139**(2), 320–324 (2005).
- A. J. Sit et al., "Sustained effect of travoprost on diurnal and nocturnal intraocular pressure," *Am. J. Ophthalmol.* **141**(6), 1131–1133 (2006).
- T. Realini, R. N. Weinreb, and S. R. Wisniewski, "Diurnal intraocular pressure patterns are not repeatable in the short term in healthy individuals," *Ophthalmology* **117**(9), 1700–1704 (2010).
- T. Realini, R. N. Weinreb, and S. Wisniewski, "Short-term repeatability of diurnal intraocular pressure patterns in glaucomatous individuals," *Ophthalmology* **118**(1), 47–51 (2011).
- R. N. Weinreb and P. L. Kaufman, "Glaucoma research community and FDA look to the future, II: NEI/FDA Glaucoma Clinical Trial Design and Endpoints Symposium: measures of structural change and visual function," *Invest. Ophthalmol. Vis. Sci.* **52**(11), 7842–7851 (2011).
- F. A. Medeiros et al., "Combining structural and functional measurements to improve estimates of rates of glaucomatous progression," *Am. J. Ophthalmol.* **153**(6), 1197–1205 (2012).
- C. K. Leung et al., "Retinal nerve fiber layer imaging with spectral-domain optical coherence tomography: patterns of retinal nerve fiber layer progression," *Ophthalmology* (in press, 2012).
- K. Mansouri et al., "Assessment of rates of structural change in glaucoma using imaging technologies," *Eye* **25**(3), 269–277 (2011).
- W. M. Grant, "Further studies on facility of flow through the trabecular meshwork," *Arch. Ophthalmol.* **60**(4), 523–533 (1958).
- W. M. Grant, "Facility of flow through the trabecular meshwork," *Arch. Ophthalmol.* **54**(2), 245–248 (1955).
- M. A. Johnstone, "The aqueous outflow system as a mechanical pump: evidence from examination of tissue and aqueous movement in human and non-human primates," *J. Glaucoma.* **13**(5), 421–438 (2004).
- M. A. Johnstone, "A new model describes an aqueous outflow pump and explores causes of pump failure in glaucoma," in *Glaucoma. Essentials in Ophthalmology*, F. Grehn and R. Stamper, Eds., pp. 3–34, Springer, Berlin, Heidelberg (2006).
- M. A. Johnstone, "Aqueous humor outflow system overview," in *Becker-Shaffer's Diagnosis and Therapy of the Glaucomas*, G. K. Kriegstein and R. N. Weinreb, Eds., pp. 25–46, Springer, Berlin, Heidelberg St. Louis, Mo (2009).
- M. Johnstone, E. Martin, and A. Jamil, "Pulsatile flow into the aqueous veins: Manifestations in normal and glaucomatous eyes," *Exper. Eye Res.* **92**(5), 318–327 (2011).
- C. K. Bahler et al., "Trabecular bypass stents decrease intraocular pressure in cultured human anterior segments," *Am. J. Ophthalmol.* **138**(6), 988–994 (2004).
- J. Ren et al., "Ex vivo optical coherence tomography imaging of collector channels with a scanning endoscopic probe," *Invest. Ophthalmol. Vis. Sci.* **52**(7), 3921–3925 (2011).
- K. W. Ascher, "Glaucoma and the aqueous veins," *Am. J. Ophthalmol.* **25**(11), 1309–1315 (1942).
- H. Goldmann, "Abfluss des Kammerwassers beim Menschen," *Ophthalmologica* **111**(2–3), 146–152 (1946).
- R. Stegmann, A. Pienaar, and D. Miller, "Viscocanalostomy for open-angle glaucoma in black African patients," *J. Cataract. Refract. Surg.* **25**(3), 316–322 (1999).
- M. R. Hee et al., "Optical coherence tomography of the human retina," *Arch. Ophthalmol.* **113**(3), 325–332 (1995).
- M. E. van Velthoven et al., "Recent developments in optical coherence tomography for imaging the retina," *Prog. Retin. Eye Res.* **26**(1), 57–77 (2007).

44. S. Asrani et al., "Detailed visualization of the anterior segment using fourier-domain optical coherence tomography," *Arch. Ophthalmol.* **126**(6), 765–771 (2008).
45. P. H. Tomlins and R. K. Wang, "Theory, developments and applications of optical coherence tomography," *J. Phys. D Appl. Phys.* **38**(15), 2519–2535 (2005).
46. T. Usui et al., "Identification of Schlemm's canal and its surrounding tissues by anterior segment fourier domain optical coherence tomography," *Invest. Ophthalmol. Vis. Sci.* **52**(9), 6934–6939 (2011).
47. Y. Yasuno et al., "Visibility of trabecular meshwork by standard and polarization-sensitive optical coherence tomography," *J. Biomed. Opt.* **15**(6), 061705 (2010).
48. L. Kagemann et al., "Identification and assessment of Schlemm's canal by spectral-domain optical coherence tomography," *Invest. Ophthalmol. Vis. Sci.* **51**(8), 4054–4059 (2010).
49. G. Shi et al., "Morphometric measurement of Schlemm's canal in normal human eye using anterior segment swept source optical coherence tomography," *J. Bio. Optics* **17**(1), 016016 (2012).
50. L. Kagemann et al., "3D visualization of aqueous humor outflow structures in-situ in humans," *Exp. Eye Res.* **93**(3), 308–315 (2011).
51. P. Li et al., "In vivo microstructural and microvascular imaging of the human corneo-scleral limbus using optical coherence tomography," *Biomed. Opt. Express* **2**(11), 3109–3118 (2011).
52. K. Singh et al., "Measurement of ocular fundus pulsation in healthy subjects using a novel Fourier-domain optical coherence tomography," *Invest. Ophthalmol. Vis. Sci.* **52**(12), 8927–8932 (2011).
53. N. Dragostinoff et al., "Depth-resolved measurement of ocular fundus pulsations by low-coherence tissue interferometry," *J. Bio. Optics* **14**(5), 054047 (2009).
54. K. Singh et al., "Development of a novel instrument to measure the pulsatile movement of ocular tissues," *Exp. Eye Res.* **91**(1), 63–68 (2010).
55. R. K. Wang, Z. Ma, and S. J. Kirkpatrick, "Tissue Doppler optical coherence elastography for real time strain rate and strain mapping of soft tissue," *Appl. Phys. Lett.* **89**(14), 144103 (2006).
56. Y. Zhao et al., "Phase-resolved optical coherence tomography and optical Doppler tomography for imaging blood flow in human skin with fast scanning using speed and high velocity sensitivity," *Opt. Lett.* **25**(2), 114–116 (2000).
57. R. K. Wang and Z. Ma, "Real-time flow imaging by removing texture pattern artifacts in spectral-domain optical Doppler tomography," *Opt. Lett.* **31**(20), 3001–3003 (2006).
58. R. K. Wang, S. Kirkpatrick, and M. Hinds, "Phase-sensitive optical coherence elastography for mapping tissue microstrains in real time," *Appl Phys. Lett.* **90**(16), 164105 (2007).
59. R. K. Wang, "Modelling optical properties of soft tissue by fractal distribution of scatterers," *J. Modern Optics* **47**(1), 103–120 (2000).
60. P. Li et al., "Assessment of strain and strain rate in embryonic chick heart in vivo using tissue Doppler optical coherence tomography," *Phys. Med. Biol.* **56**(22), 7081–7092 (2011).
61. B. A. Smit and M. A. Johnstone, "Effects of viscoelastic injection into Schlemm's canal in primate and human eyes: potential relevance to viscocanalostomy," *Ophthalmology* **109**(4), 786–792 (2002).
62. D. F. Woodward, A. H.-P. Krauss, and S. F. E. Nilsson, "Bimatoprost effects on aqueous humor dynamics in monkeys," *J. Ophthalmol.* **2010**, 926192 (2010).
63. C. B. Toris et al., "Aqueous humor dynamics in monkeys with laser-induced glaucoma," *J Ocular Pharm Therapeutics: the Official Journal of the Association for Ocular Pharmacology and Therapeutics* **16**(1), 19–27 (2000).
64. M. A. Johnstone and W. G. Grant, "Pressure-dependent changes in structures of the aqueous outflow system of human and monkey eyes," *Am. J. Ophthalmol.* **75**(3), 365–383 (1973).
65. M. A. Johnstone, "Pressure-dependent changes in nuclei and the process origins of the endothelial cells lining Schlemm's canal," *Invest. Ophthalmol. Vis. Sci.* **18**(1), 44–51 (1979).
66. N. Ehlers, T. Bramsen, and S. Sperling, "Applanation tonometry and central corneal thickness," *Acta. Ophthalmol.* **53**(1), 34–43 (1975).
67. M. C. Grieshaber et al., "Effect of central corneal thickness on dynamic contour tonometry and Goldmann applanation tonometry in primary open-angle glaucoma," *Arch. Ophthalmol.* **125**(6), 740–744 (2007).
68. Y. Gelaw et al., "The influence of central corneal thickness on intraocular pressure measured by goldmann applanation tonometry among selected Ethiopian communities," *J. Glaucoma* **19**, 514–518 (2010).
69. P. Fogagnolo et al., "Test-retest variability of intraocular pressure and ocular pulse amplitude for dynamic contour tonometry: a multicentre study," *Br. J. Ophthalmol.* **94**(4), 419–423 (2010).
70. R. K. Wang et al., "Three dimensional optical angiography," *Opt. Express* **15**(7), 4083–4097 (2007).
71. L. An, T. T. Shen, and R. K. Wang, "Using ultrahigh sensitive optical microangiography to achieve comprehensive depth resolved microvasculature mapping for human retina," *J. Biomed. Optics* **16**(10), 106013 (2011).